Time-of-flight radio-frequency mass separator for continuous low-energy ion beams

Andrew J. Keller [a,b] Georg Bollen [a,*]

[a] *Department of Physics and Astronomy & National Superconducting Cyclotron Laboratory, Michigan State University, East Lansing, MI, USA*

[b] *Honors College, Michigan State University, East Lansing, MI, USA*

Abstract

A novel concept for a time-of-flight radio-frequency mass separator for low-energy beams is investigated. The concept is based on two sets of deflectors with sinusoidally-varying applied voltage and at least one Einzel lens. Results of analytical calculation and numerical simulation are presented and compared. Potential advantages of such a scheme include a resolving power similar to that of simple electromagnetic separators while at lower costs, as well as the possibility to incorporate the scheme relatively easily into existing electrostatic beam transport systems.

Key words: mass separation, time of flight, radio-frequency, ion beam optics
PACS: 07.75.+h, 82.80.Rt

1 Introduction

The separation of ions with different charge-to-mass ratios q/m is important in physics, chemistry, and many other areas of research and application. Various mass separation techniques exist and the choice of which technique to employ depends on the beam properties of the ions to be separated and the desired resolving power. Classical electromagnetic separators make use of the difference in the rigidity of ions in magnetic fields and are, for example, used for the separation of isotopes [1]. Linear radio-frequency (RF) quadrupole mass filters [2] or similar ion trap devices make use of mass-dependent motional instabilities to separate ions. They are widely applied in analytical chemistry or in the

* MSU/NSCL, 1 Cyclotron, East Lansing, MI 48824, USA; phone (517) 333-6435
Email addresses: keller34@msu.edu (Andrew J. Keller), bollen@nscl.msu.edu (Georg Bollen).

form of residual gas analyzers. High resolution mass separation can be performed in Penning traps by making use of the difference in the ions' cyclotron frequencies; resolving powers sufficient to separate isobars [3] or even nuclear isomers [4] are achieved. High resolution mass separation of continuous beams is also obtained in Smith-type RF mass spectrometers [5,6]. Ions injected into the system perform two cyclotron orbits in a magnetic field. Passing twice through an RF acceleration cavity they are only transmitted if the change in beam energy is compensated in the second turn. In the case of pulsed ion beams with constant energy the time of flight of ions can be utilized to achieve mass separation. Such a separation is for example utilized in RF separators for high-energy (> 50 MeV/nucleon) rare isotope beams [7,8]. These devices make use of a beam's time structure that has been imprinted by the acceleration process and the time-of-flight difference after a drift length where the ions pass through a high-voltage radiofrequency beam deflector.

In this paper we evaluate and discuss a concept to mass-separate continuous low-energy ion beams of energies in the range of a few keV to tens of keVs using a combined RF and time-of-flight technique. This scheme shares similarities with the RF separator for high-energy beams and the RF Smith spectrometer mentioned above. The simplicity of the technique and the possibility of implantation in existing electrostatic ion beam transport systems make this technique interesting.

2 TOF-RF mass separation

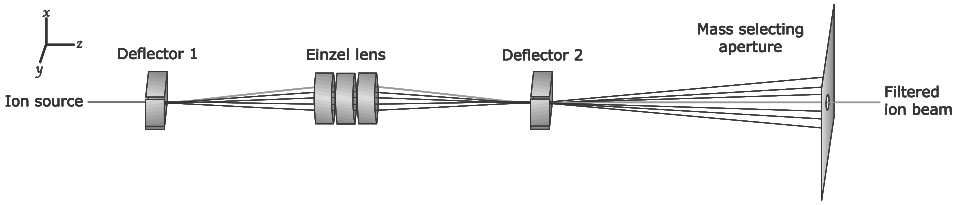

Fig. 1. Schematic for a time-of-flight radio-frequency (TOF-RF) mass separator for continuous low-energy ion beams. This schematic shows a system with the minimum number of necessary components.

The concept of time-of-flight radio-frequency (TOF-RF) mass separation is illustrated in figure 1. Stated in the order in which an ion would encounter them, the system consists of a beam deflector, an Einzel lens, another beam deflector, and a mass-selecting aperture. It should be noted that the sequence of such ion optical elements is typical for a section of an electrostatic beam transport system for ion beams with energies below a few tens of keV. Each set of the deflectors shown consists of two orthogonal pairs of deflection plates, one for deflection in the x-direction and one for the y-direction with respect to the coordinate system used in the figure. To the two x-deflection plates of both

the entrance and exit deflectors, RF voltages $u_x(t) = u_0 \sin(\omega t)$ and $-u_x(t)$ are applied. Similarly, to the y-deflector plates of both deflectors, RF voltages $u_y(t) = u_0 \sin(\omega t + \pi/2)$ and $-u_y(t)$ are applied, phase shifted by 90 degrees with respect to those applied to the x-deflector plates. The Einzel lens in the center between both deflectors focuses a beam leaving the first deflector onto the entrance of the second deflector, i.e. the ion trajectories make the same angle with respect to the z-axis as they did upon leaving the first deflector. The aperture, a circular hole centered on the z-axis, stops ions that are further away from the beam axis than the inner radius of the aperture.

We will first consider what happens using just the x-deflectors, which means no RF voltage will be applied to the y-deflectors. Ions of differing mass streaming continuously into the system with the same energy will have different velocities. Because of the electric field generated by the sinusoidally-varying voltage u_x discussed previously, these ions will be accelerated at the first deflector according to their mass and when they arrive. The ions then drift with constant but mass dependent velocity until they reach the Einzel lens, whereupon they are focused into the second deflector. In the second deflector, the ions will again be accelerated. If the time an ion takes to go from the start of the first deflector to the start of the second deflector is an integer multiple of the period of the sinusoidal voltage, then the second deflector will accelerate the ions the same as previously, thus reversing any trajectory changes made by the first deflector. This time of flight is mass dependent, so only ions with a certain charge to mass ratio will satisfy this condition. For ions with the wrong q/m ratio the trajectory changes will not be entirely reversed and the beam deflection may even be exaggerated. The ions will continue their path until they reach the aperture position. Those with the correct q/m ratio will pass the aperture because their direction is parallel and they are close to the z-axis of the system. Ions with the wrong q/m ratio will behave differently. At the position of the aperture their beam will sweep up and down along a line $y = 0$ in the xy plane, according to their mass and when they entered the system. Since they sweep over the aperture a fraction of the wrong ions will still be transmitted, which is not desirable.

In order to avoid the transmission of these wrong ions the y-deflectors are employed by applying an RF voltage u_y as discussed above. With u_x and u_y being out of phase by ninety degrees, the ions will form circular orbits at the aperture according to their mass. The time at which the ions enter the system becomes inconsequential, or in other words, ions of a particular mass will always be seen at a certain distance from the z-axis at the aperture. It is in this way that the system works with continuous ion beams, and furthermore, the time-of-flight of an ion and the RF-voltage applied to the deflectors primarily determines the separation.

3 Analytical description

In the following analytical description of the TOF-RF concept simplifying assumptions are made. First, the electric field generated by each pair of deflector plates is considered uniform inside the deflectors and non-existent outside of them. Second, the Einzel lens is approximated by a thin lens centered between the two deflectors. Third, we assume no energy spread. Finally, we assume a beam with no emittance. It is clear that the real system will show deviations from this simplified scheme. The effects have been analyzed via computer simulations and the results are discussed in section 4. The coordinate system used for the analytical description is the same as the coordinate system shown in figure 1. For simplification we will first consider one pair of deflectors per deflector assembly. The results are trivially generalized later.

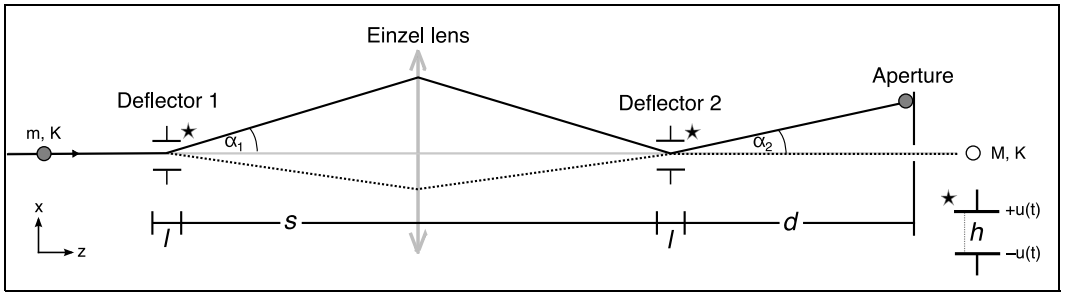

Fig. 2. Diagram displaying most of the variables used in the analytical description.

Figure 2 shows many of the variables used in the analytical description. As shown in the diagram, arbitrary ions with mass m and charge q come in to the system with kinetic energy K in the +z-direction. Both deflectors have length l and plate separation h. The drift region between the first and second deflectors has length s, and the drift region between the second deflector and the aperture has length d. The angle that an ion trajectory makes with the z-axis upon exiting the first deflector is denoted by α_1, and likewise the angle upon leaving the second deflector is denoted by α_2. By an appropriate choice of ω, the angular frequency of the sinusoidal voltage, we admit ions of mass $m = M$ and energy K to pass through the aperture. Of the variables that are not pictured, V is the amplitude and n is the harmonic number of the sinusoidal voltage. The initial x-velocity is denoted by v_{xo} and the initial x-displacement is denoted by x_0. Finally, a phase shift for the sinusoidal voltage is denoted by ϕ.

Table 1 lists the main parameters used in the calculations and numerical simulations unless explicitly specified otherwise. Most of the length parameters were motivated by the dimensions of similar components currently in use at the LEBIT facility [9] at the NSCL. The lens voltages required for obtaining the desired focussing properties were obtained in the numerical beam transport simulations.

Table 1
Parameters used in the analytical calculations and numerical simulations.

Ion mass to be transmitted M	50 u	RF amplitude V	200 V
Ion charge q	1 e	Deflector plate separation h	0.035 m
Ion's kinetic energy K	5000 eV	Length of deflector plate l	0.020 m
Initial v_{xo}	0 m/s	Distance between deflectors s	1.58 m
Initial x_o	0 m	Drift length before aperture d	1.49 m
Phase shift ϕ	0	Harmonic number n	10
Einzel lens voltage V_{Einzel}	+2755 V	Einzel lens inner diameter	74.4 mm
		Einzel lens central tube length	71.3 mm

The time it takes for an ion of mass M, which is to be transmitted, to pass from the start of deflector 1 to the start of deflector 2 is given by $(l+s)/v_z$, where $v_z = \sqrt{2K/M}$ is the initial velocity in the +z-direction. For the example given in table 1, this time of flight is about 11 μs. If the period of the sinusoidal voltage curve is given by $T = 2\pi/\omega = (l+s)/(nv_z)$, an ion of mass M will come into the second deflector exactly in phase as discussed in section 2. This means that the angular frequency for which this can be achieved is given by $\omega = 2\pi n v_z/(l+s)$. With the parameters given in table 1, this leads to a frequency of $\omega/(2\pi) = 868$ kHz. Since we assume no energy spread, the angular frequency $\omega \propto 1/\sqrt{M}$ depends primarily on our selected mass M for any given setup.

3.1 The first deflector

The acceleration and velocity of an ion of mass m and charge q inside the first deflector is given by

$$a_x = \eta \sin(\omega t + \phi) \tag{1}$$

$$v_{x1} = v_{xo} + \frac{\eta}{\omega}\left[\cos(\phi) - \cos(\omega t + \phi)\right], \tag{2}$$

with $\eta \equiv (2Vq)/(hm)$. The velocity in the x-direction at the end of the first deflector (after a time $t = l/v_z$) is

$$v_{x1f} = v_{xo} + \frac{\eta}{\omega}\left(\cos(\phi) - \cos(l\mu + \phi)\right), \tag{3}$$

with $\mu \equiv \omega/v_z$.

Figure 3 shows the angle $\alpha_1 = \arctan(v_{x1f}/v_z)$ as obtained from equation 3 and the values from table 1 using the values stated earlier as a function of the mass m of the ions. The angle of the ions with mass number A = 50 to be transmitted is marked with intersecting dashed lines. The shapes of the graphs are dependent upon the value of ϕ used. For instance, with $\phi = \pi$, i.e. reversing the polarity of the RF field, the graph is the same as for $\phi = 0$ except for with negative α_1.

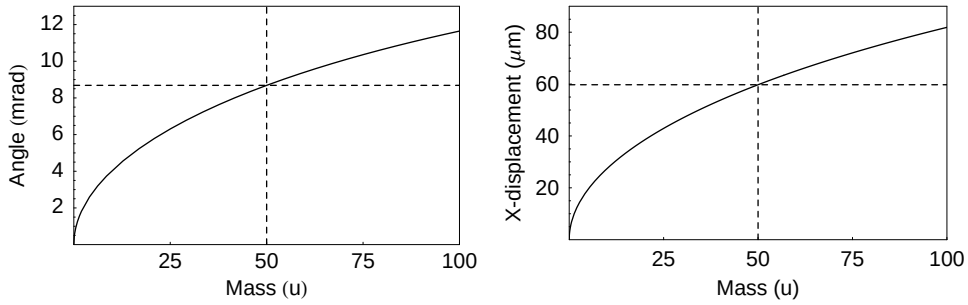

Fig. 3. The angle α_1 (left) and x-displacement (right) at the end of the first deflector for ions of differing mass for the parameters as listed in table 1 and for an RF phase $\phi = 0$.

The x-displacement of an ion of mass m inside the deflector is given by

$$x_1 = x_o + [v_{xo} + \frac{\eta}{\omega}\cos\phi]t + \frac{\eta}{\omega^2}[\sin\phi - \sin(\omega t + \phi)] \tag{4}$$

The displacement at the end of the deflector is

$$x_{1f} = x_o + \frac{v_{xo}l}{v_z} + \frac{\eta}{\omega^2}\left[l\mu\cos\phi + \sin\phi - \sin\left(l\mu + \phi\right)\right] \tag{5}$$

Figure 3 shows this x-displacement as a function of the mass m of the ions. The case of the A = 50 ion is marked with intersecting dashed lines. Again, the shape is highly dependent upon the chosen phase ϕ.

3.2 The Einzel lens

As briefly stated previously, the Einzel lens is assumed to be a thin lens located halfway between the two deflectors. The purpose of this lens is to focus the ion beam such that the ions all enter the second deflector making an angle with the z-axis equal to α_1. This also implies that the displacement from the z-axis at the end of the first deflector will be the same as the displacement from the z-axis at the start of the second deflector for any ion. No further considerations of the lens are accounted for in the analytical treatment.

3.3 The second deflector

We can find the x-velocity of an ion inside the second deflector by using equation 2 as before but instead accounting for a different phase shift. This new phase shift is given by $\phi' = \phi + \omega(l+s)/v_z$. Since ϕ' accounts for the ion's prior time-of-flight, the t in the following equations will represent the time since an ion has entered the second deflector, not the time since the ion has entered the first deflector. Also, note that at the start of the second deflector the ion will have an initial x-velocity of $-v_{x1f}$. The x-velocity for an ion inside the second deflector is

$$v_{x2} = \frac{\eta}{\omega}\left[\cos\phi' - \cos\left(\omega t + \phi'\right)\right] - v_{x1f} \tag{6}$$

The x-velocity at the end of this deflector is

$$v_{x2f} = \frac{\eta}{\omega}\left[\cos(\mu(l+s)+\phi) - \cos(\mu(2l+s)+\phi)\right] - v_{x1f} \tag{7}$$

Figure 4 shows the resulting angle $\alpha_2 = \arctan(v_{x2f}/v_z)$ (see figure 2) as a function of mass m for different harmonics n of the frequency used. Notice that as we increase the harmonic number, the difference in angle of nearby masses becomes greater. A higher harmonic number also results in a trend away from symmetry about $\alpha_2 = 0$ over this mass range. This trend is just a consequence of choice of $\phi = 0$. Similarly to figure 3, the choice of $\phi = \pi$ would invert the graph, here resulting in a trend toward positive values. Higher harmonic numbers result in a steeper trend away from symmetry due to increased sensitivity to relative phase shift between the first and second deflector for heavier masses. The most important observation is that for A = 50 the angle $\alpha_2 = 0$. This means the ions leave the second deflector, as desired, without deflection.

The x-displacement of an ion in the second deflector is

$$x_2 = x_{1f} - v_{x1f}t + \frac{\eta t}{\omega}\cos\phi' + \frac{\eta}{\omega^2}\left[\sin\phi' - \sin(\omega t + \phi')\right] \tag{8}$$

Evaluating equation 8 at $t = l/v_z$, we find that for A = 50 ions, having zero velocity in the x-direction, a small but non-zero displacement in the x-direction is observed. Figure 5 shows the x-displacement for ions of differing mass after the second deflector. Intersecting dashed lines indicate the displacement of A = 50 ions. It can be seen that the magnitude of the displacement of A = 50 ions increases with higher harmonics, which is again a consequence of the time-dependent fields.

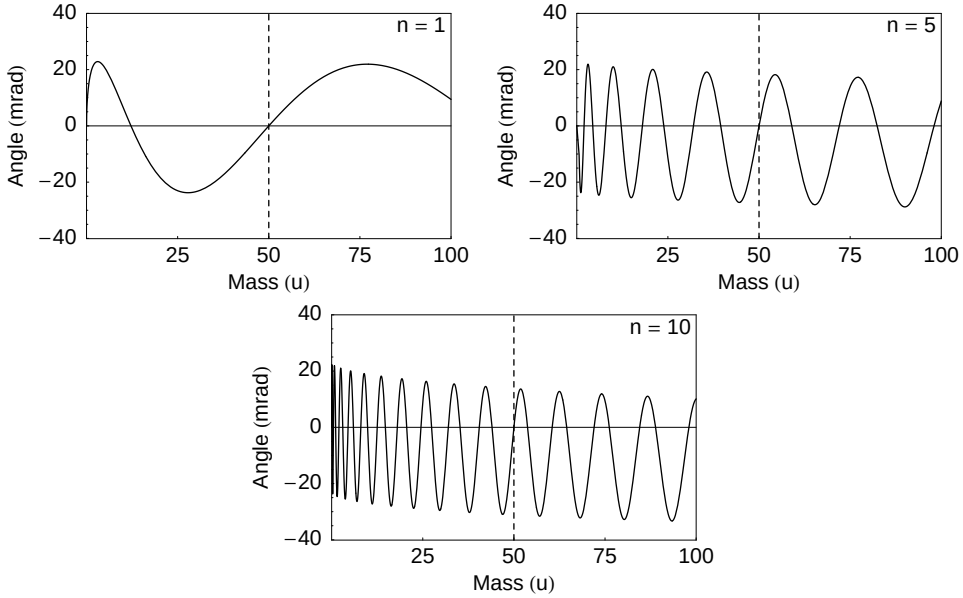

Fig. 4. The angle α_2 at the end of the second deflector for ions of differing mass for the parameters listed in table 1, except with n =1, 5, and 10.

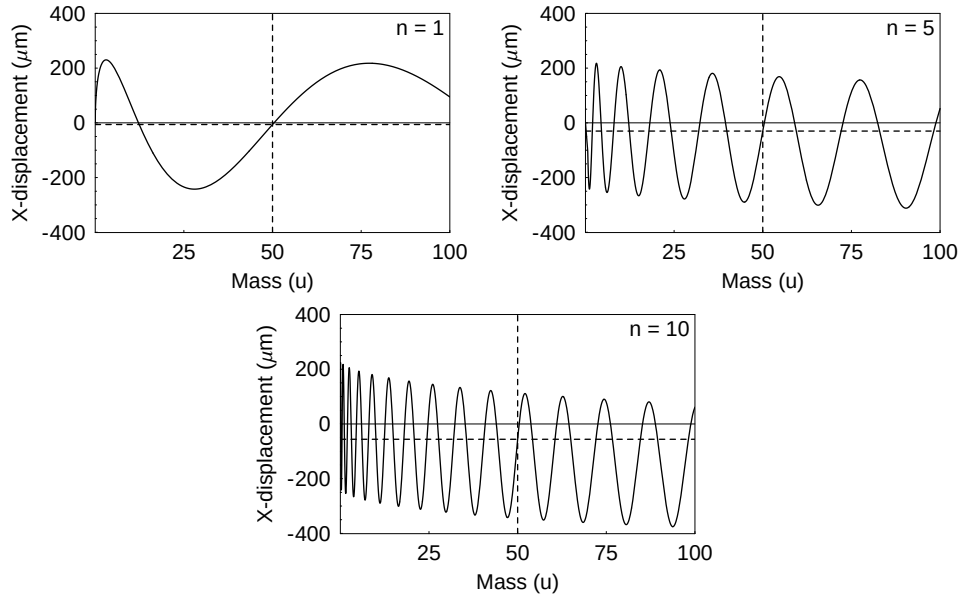

Fig. 5. The x-displacement at the end of the second deflector for ions of differing mass for the parameters listed in table 1, except with n = 1, 5, and 10.

3.4 Ion distribution at the end of the drift section

Here we reintroduce the y-deflector pairs not used so far. Their effect is described by equations 7 and 8 with the exception that ϕ needs to be replaced by $\phi + \frac{\pi}{2}$. The resulting set of four equations for the x and y dimensions completely determine the location of ions at a distance d away from the end of

the second deflector. Allowing the phase ϕ, which only depends on the time of arrival of the ions at the first deflector with respect to the phase of the applied RF voltage, to vary freely, we expect the ions with masses $m \neq M$ to appear as circles of various radii at the aperture according to their mass. Figure 6 shows that this indeed happens. The A = 50 ions arrive at nearly a point on the z-axis due to their negligible displacement. Each concentric circle around the center represents ions with a mass number A decreased by one. For ions with A > 50 (omitted for clarity) the corresponding circles would also increase in diameter. Figure 6 shows that with increasing harmonic number the angular separation (and thus the radial separation after a drift region) between different masses increases. However, the figure also shows that a maximum deflection is eventually reached. In the case of $n = 10$, the circle formed by the A = 45 ions is such a maximum. The circles for A = 44 ions (not shown in the figure) and A = 46 ions have a similar but somewhat smaller diameter. In other words, with an increase in the harmonic number n, the nearest maximum in deflection will belong to a mass number closer to the selected ion's mass number A, already indicating that more ion species with several q/m ratios can be transmitted.

In order to analyze this we will think of 'transmitted ions' as the ions which exit the second deflector without being deflected away from the z-axis. It is easy to see that in addition to our selected ions with mass $m = M$, ions with a time-of-flight corresponding to a harmonic of the frequency used will be transmitted as well. We will first concern ourselves with the ions transmitted whenever $\omega(l + s)/v_z$ is an integer multiple of 2π. This is the case for

$$m = \left\{ \frac{k^2 M}{n^2} \middle| k \in \mathbb{Z}^+ \right\} \tag{9}$$

Ions with these masses are always transmitted. For example, when $A = 50$ and $n = 10$, $A = \{32.0, 40.5, 50.0, 60.5, 72.0\}$ are expected to be transmitted, among ions with other mass numbers.

In the case that ions experience an integer multiple of the full RF period within the deflector, they will not be deflected and instead pass straight through the system. This could pose a problem for the system if the distance s between the deflectors was chosen to be small compared to l. The masses for which this could occur are given by

$$m = \left\{ \frac{k^2 M}{n^2} \left(\frac{l + s}{l} \right)^2 \middle| k \in \mathbb{Z}^+ \right\} \tag{10}$$

However, under common conditions, this situation will only occur for very heavy masses. For example, given the parameters in table 1, only ions with

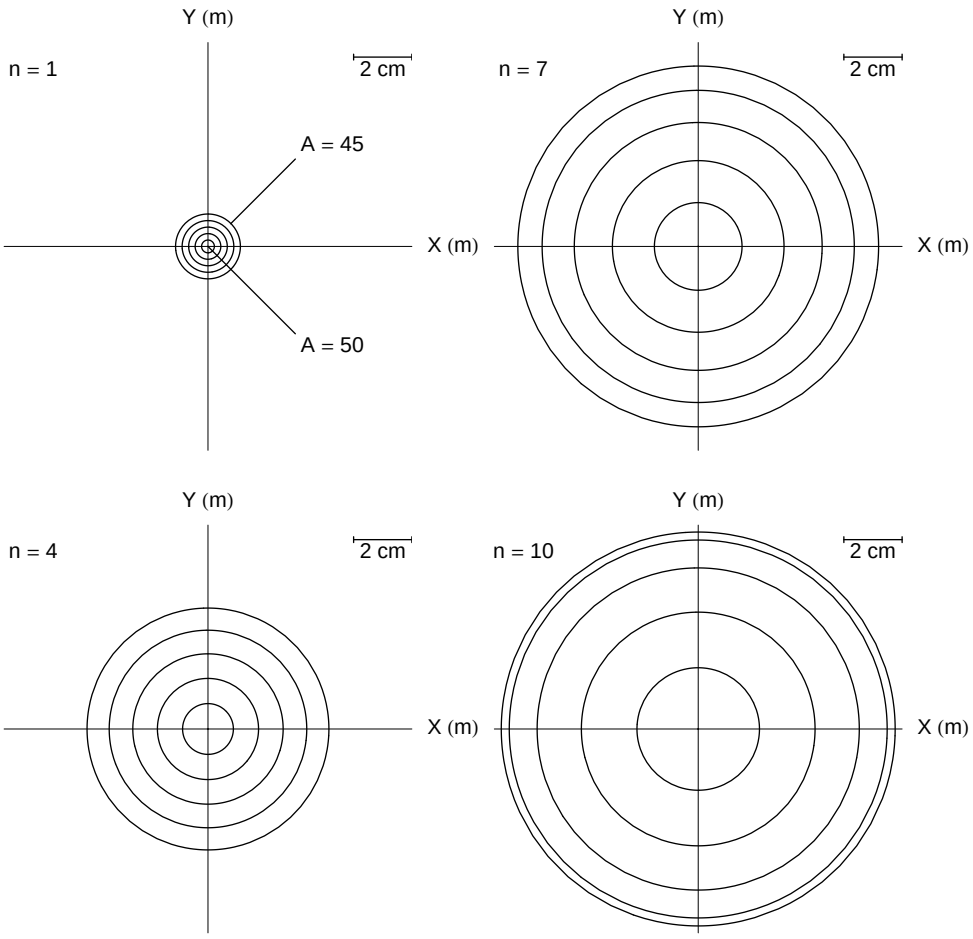

Fig. 6. From the outside circle to the inside circle, we start with the ion group A = 45 and increase in mass number by one until the inner circle. The very center of the graph represents the A = 50 ions for which we are selecting. Each graph represents a different choice of harmonic.

mass numbers $A > 3000$ could pass through the system in this way.

4 Numerical simulation

In order to test the radio-frequency time-of-flight concept under conditions more realistic than those assumed above, numerical simulations were performed. The ion motion through the system was investigated by using the SIMION v7.0 software for the calculation of electric potentials and ray-tracing. For the determination of the electric fields inside the deflectors, electrode geometry was used similar to that currently in use at the LEBIT facility [9] at the NSCL. In the numerical simulations two Einzel lenses were used instead of only one for refocusing the ion beams. This allows for minimizing the maximum beam displacement from the z-axis and provides more flexibility

in a possible implementation. The layout of the system simulated, including specific locations of the components, is shown in figure 7.

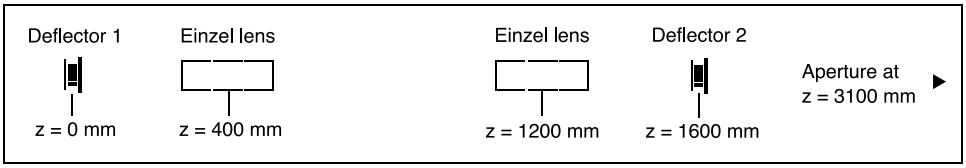

Fig. 7. A schematic of the TOF-RF mass separator as simulated in SIMION v7.0. Ions enter from the left.

In our numerical simulations we used the same parameters as for the analytical study and the additional parameters needed for the description of the Einzel lens, which are also provided in table 1. The voltages for the Einzel lenses were found with SIMION and provide for a beam roughly parallel between the two lenses. For the beam properties we assume an emittance of 15π mm mrad and a beam diameter of 1 cm at the start of the first deflector. The beam was monoenergetic, which means that the energy spread in the beam is small enough ($\Delta E/E$ well below $< 1\%$) not to limit the resolving power. This is critical, as the analytical description predicts that when $\Delta E/E$ is 2%, the energy spread begins to become large enough that the final trajectories of some A = 50 ions would be indistinguishable from those of A = 51 ions. In order to determine the RF frequency that leads to transmission for our reference ion with mass number A = 50, the time of flight from one deflector to the other needs to be known. In contrast to the analytical simulation, the effect of the change in kinetic energy inside the Einzel lenses needs to be considered. Therefore the time of flight was determined by running a zero-emittance beam through the system. The obtained value leads to an RF frequency of $\omega/(2\pi) =$ 835020 Hz when we again choose the tenth harmonic for obtaining a greater resolving power. This is about 3.8% smaller than the one obtained analytically which can be explained by the decreased ion velocity inside the Einzel lens. 1000 ions were run through the system for each mass between A = 45 and A = 55 and their displacement from the z-axis at the position of the aperture was recorded. Figure 8 shows the resulting circular spatial distributions for the different masses. The superimposed solid circles correspond to those already shown are shown figure 8 but reduced in size by a factor of 0.72. This scaling of the theoretical predictions corrects for the simplified assumptions of the electric field inside the deflector (sharp cut off, no mutual shielding of the x and y deflector pairs). Using this scaling good agreement is observed between the analytical predictions and the numerical simulations.

Figure 8 shows that the A = 50 ions are well separated from the nearest masses (A = 49, 51). Figure 9 provides a corresponding number density plot for the transverse displacement of the ions. From the figures it becomes clear that a circular aperture can be used to completely separate the wrong ions from the A = 50 ions.

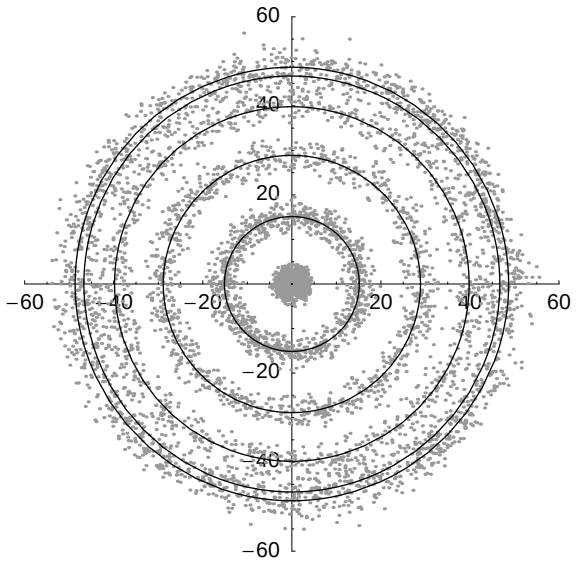

Fig. 8. The location of simulated ions with $45 \leq A \leq 50$ at the aperture ($A > 50$ not included for sake of comparison). The sharp lines represent the theoretical expected locations of the different mass groups, starting with $A = 45$ on the outside and progressing inward to the center point where $A = 50$.

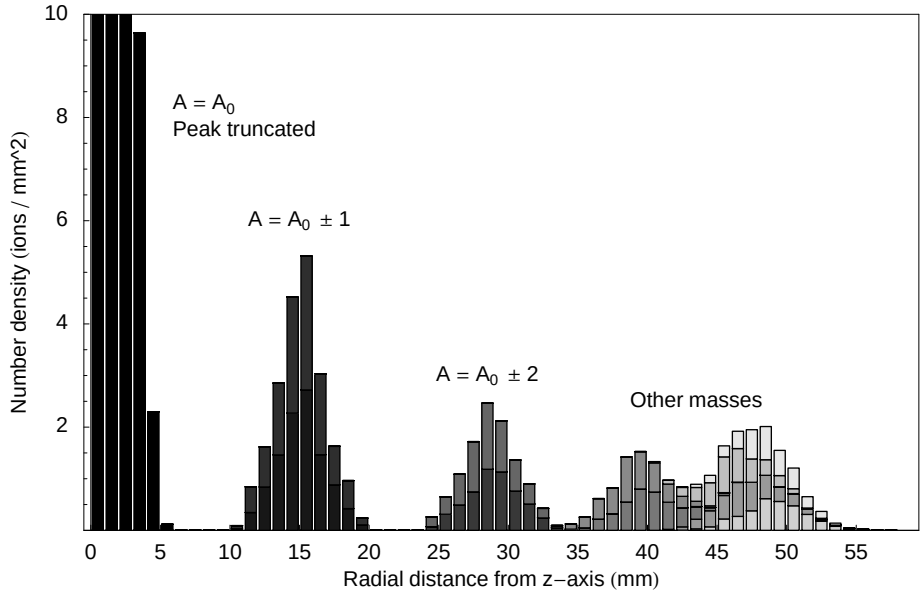

Fig. 9. Number density vs. radial distance from z-axis for ions near $A_0 = 50$ arriving at the aperture position. For the first bin which includes the $A = 50$ ions that fall closest to the axis, the beam density is more than 50 count/mm^2.

All distributions including the central peak for the $A = 50$ ions (truncated in the figure) are found to be well described by Gaussians. The central peak corresponds to a two-dimensional Gaussian distribution while the other distributions have azimuthal symmetry and a Gaussian profile in the radial direction. In order to obtain a value for the resolving power of the system we determined

by Gaussian fits the width Δr (FWHM) of the A = 50 ion distribution as well as the center value $\bar{r}$ of the A = 51 ion distribution for the displacement from the z-axis.

From figure 6, it is apparent that the radial distance from the z-axis of ion distributions scales linearly to a first-order approximation with the mass difference to the ions in the central peak, so it is justifiable to define a spectrometric resolving power of this system as $R = \bar{r}/\Delta r \cdot A$. For the A = 50 case shown in figure 9 we obtain a value of $R = 200(9)$.

The resolving power just introduced ignores the effect of an aperture that would be required for the actual mass separation and which, assuming Gaussian beam profiles, will always limit the transmission through the system. In order to obtain a desired transmission probability T the radius of the central aperture needs to be $\tilde{r} = \sigma\sqrt{2\log(1/(1-T))}$. Therefore, the resolving power for mass separation $R^* = \bar{r}A/(2\tilde{r})$. At 50% transmission, the required radius of the aperture is simply $1/2 \cdot \Delta r$ (FWHM), and thus $R^* = R$. For 90% transmission, the resolving power decreases to $R^* = 110(5)$.

Figure 10 shows a plot of the deflection angles $q = \arctan\left(\sqrt{v_x^2 + v_y^2}/v_z\right)$ vs. the radial displacements from the z-axis. The figure illustrates the basis of the mass separation being the occurrence of different deflection angles for different masses. For shorter drift distances the spatial resolution will be reduced, while for larger distances the spatial resolution may not necessarily keep increasing for a given setup. Incomplete separation of the angles of ions with differing mass will result in a reduction in spatial resolution even with large drift distances. However, reducing the spread in the initial angles of the ions will not necessarily result in greater resolving power, as demonstrated in the next section.

5 Evaluation of achievable resolving power

A systematic exploration of the effects of beam emittance and changes of separator parameters on the spectrometric resolving power was performed. Instead of using SIMION, which would have been very time consuming, the analytical description was employed in combination with large sets of ions representing non-zero emittance beams. The parameters of table 1 were used unless specified otherwise. In order to calculate the resolving power, the center value $\bar{r}$ of the spatial ion distributions was multiplied with the scaling factor of 0.72 already used earlier to match with the results of the numerical simulation. The width Δr of the distributions was obtained from the difference between the maximum and minimum values of the displacement attained by an ion species, multiplied by a constant factor of 0.3 that was found to provide a

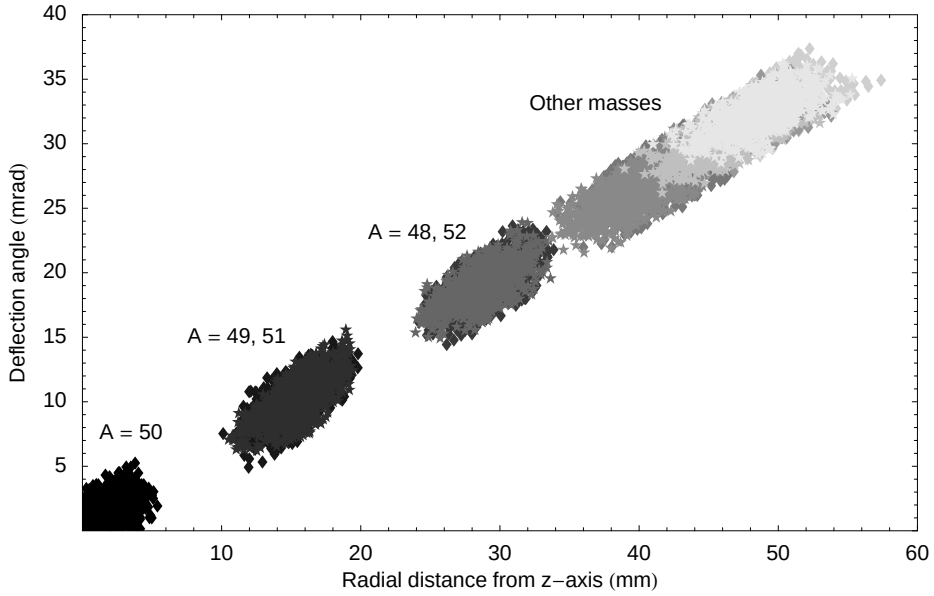

Fig. 10. Plot of the deflection angles vs. the radial displacements from the z-axis for ions with different mass.

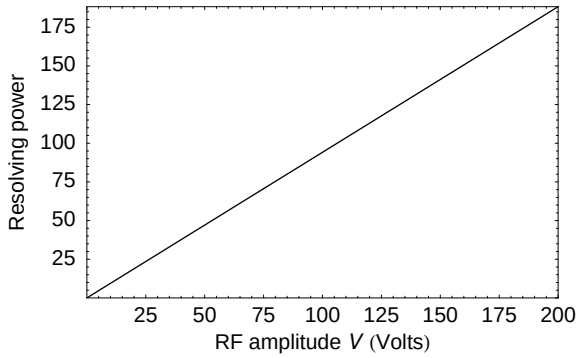

Fig. 11. Resolving power as a function of RF amplitude V applied to the deflectors.

good match with the width (FWHM) from the numerical simulation.

The relationship between RF amplitude and resolving power is linear as one might expect. This is shown in figure 11.

The beam emittance will limit the achievable resolving power. Figure 12 shows the resolving power as a function of the drift length d for various values of the beam emittance ϵ and for a constant beam divergence of 3 mrad (top) and a constant beam half-width of 5 mm (bottom). For a constant beam divergence, a lower emittance value will result in a shorter drift length d required to attain the same resolving power, and for a large drift length the resolving power approaches a constant independent of the beam emittance.

Though less intuitive, the theory suggests that a smaller deflector plate length l, or simply a larger distance s, results in greater angular separation and thus

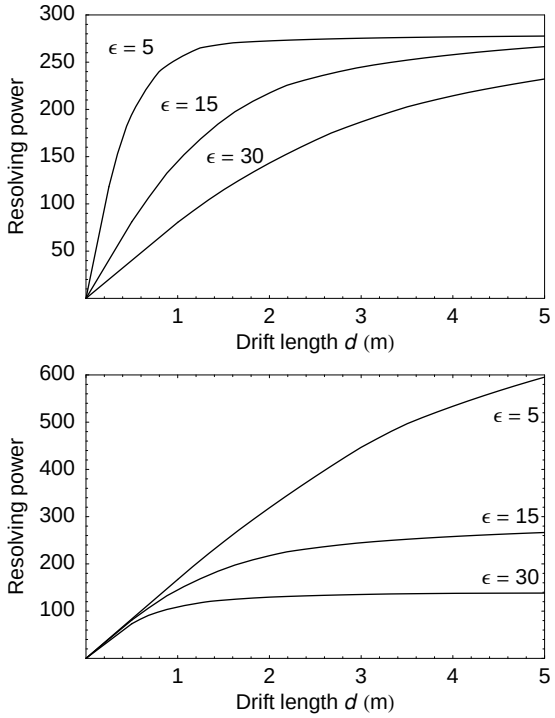

Fig. 12. Resolving power as a function of drift length d for various values of the beam emittance ϵ (given in units of π mm mrad) with beam divergence held constant (top) and with beam half-width held constant (bottom). The other parameters are set as stated in Table 1.

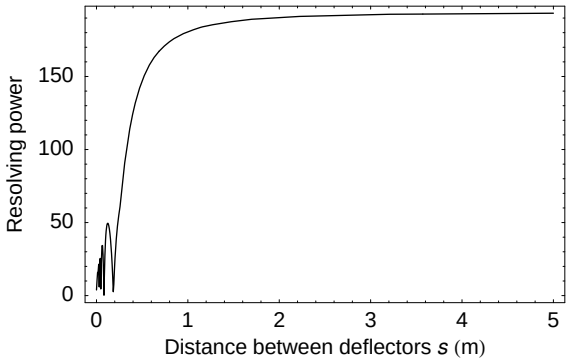

Fig. 13. The effect of increased s, or distance between deflectors, on the resolving power. The other parameters are set as stated in Table 1.

greater resolving power. For a given l, there are certain values of s, which are small in a typical implementation and are governed by equation 10, for which masses neighboring the selected mass are also transmitted. For example, when the parameters of table 1 are used in selecting for A = 50, there are several small values of s for which A = 51 is also transmitted. Specifically, equation 10 suggests that an increase in the ratio of $(l + s)/l$ will result in improved resolving power, but for a smaller l, it is clear that V must be adjusted to compensate. From figure 13 we also see that the benefit gained by shorter deflectors or longer length between deflectors has limits, however.

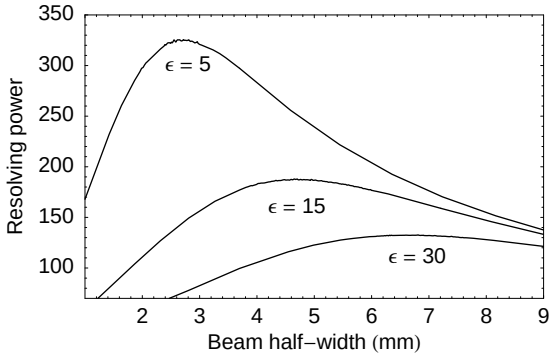

Fig. 14. Resolving power as a function of beam half-width for various values of ϵ, the beam emittance in units of π mm mrad. The other parameters are set as stated in Table 1.

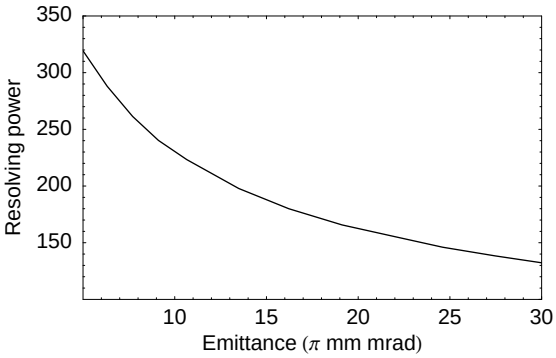

Fig. 15. Resolving power as a function of emittance given optimal beam injection. The other parameters are set according as stated in Table 1.

For a given emittance and drift length d, there is a beam half-width for which the resolving power is optimized. Figure 14 demonstrates that depending on how large the emittance is, there are significant gains in resolving power if the beam is appropriately tuned prior to entering the TOF-RF separator system. The figure also shows that the assumption of a half-width of 5 mm was a nearly optimal choice for the numerical simulations given the 15 π mm mrad beam emittance. It was found that the distance between deflectors s does not affect the value of the optimal beam half-width, but only the magnitude of the resolving power.

The evaluation of the resolving power as a function of emittance is complicated by this additional dependence on how a beam with a given emittance is injected. For various values of emittance ϵ, the beam half-widths w for which resolving power was maximized were measured and recorded. The resulting data are linear over the range $5 \leq \epsilon \leq 30$, and a linear fit was applied giving an equation of $w = 2.33 + 0.153\epsilon$, with w measured in mm and ϵ in $\pi\cdot$ mm $\cdot$ mrad. Figure 15 shows the effect of emittance on resolving power when the beam half-width is set to maximize resolving power according to this equation.

Finally, aberrations and fringe field effects are still not accounted for and could pose a problem. The theory naively says that the ultimate separation of the ions depends linearly on the strength of the electric fields in the deflectors. In reality, if the beam is deflected too much, there may be large aberrations when the beam passes the Einzel lens. However, the numerical simulations (section 3) for a realistic system have shown that resolving powers close to 200 are possible.

6 Conclusions

We have studied a time-of-flight mass separation scheme for low-energy continuous ion beams where the beams are deflected twice by spatially separated RF fields. The TOF-RF mass separator concept has interesting features. It could possibly be implemented in existing electrostatic beam transport systems, providing in-line mass separation. In the cases discussed here Einzel lenses were used but different focusing elements like electrostatic quadrupole lenses can also be used. We assumed that the RF frequency would be varied to change the mass to be transmitted. An alternative would be the use of two fixed-frequency generators and to adjust the relative RF phase. A unique feature of the system is its simultaneous transmission of different masses depending on the RF harmonics used. This can be a drawback if a large number of different masses are simultaneously delivered by the ion source. On the other hand, by appropriate choice of harmonics and frequency, two or more desired masses could be transmitted simultaneously. Finally, the resolving power that can be achieved with the proposed scheme is comparable to that obtainable with simple electromagnetic separators.

7 Acknowledgments

We wish to acknowledge the support of Michigan State University and the National Science Foundation Grant No. PHY-0110253. A.K. wished to express his gratitude to the Honors College of Michigan State University for providing a Professorial Assistantship.

References

[1] see Series of Proceedings of Int. Conf. on Electromagnetic Isotopes Separation (EMIS), published in Nucl. Instr. Meth. A

[2] P. H. Dawson, Quadrupole Mass Spectrometry and Its Applications, Elsevier, Amsterdam, 1976

[3] H. Raimbault-Hartmann et al., Nucl. Instr. Meth. B126 (1997) 378

[4] K. Blaum et al., Europhys. Lett. 67 (2004) 586

[5] L.G. Smith, Rev. Sci. Instrum. 22 (1951) 115

[6] D. Lunney et al., Phys. Rev. C 64 (2001) 054311

[7] K. Yamada, Nucl. Phys. A 746 (2004) 156

[8] D. Gorelov et al., Proc. Particle accelerator Conference 2005 (PAC2005), Knoxville, TN, May 16-20, 2005, http://accelconf.web.cern.ch/accelconf/p05/PAPERS/FPAE072.PDF

[9] R. Ringle et al., Int. Journal Mass Spectr. 251 (2006) 300